

# Approaching the Intrinsic Limit in Transition Metal Diselenides via Point Defect Control

Drew Edelberg,<sup>†,○</sup> Daniel Rhodes,<sup>‡,○</sup> Alexander Kerelsky,<sup>†</sup> Bumho Kim,<sup>‡</sup> Jue Wang,<sup>§,ID</sup> Amirali Zangiabadi,<sup>⊥</sup> Chanul Kim,<sup>⊥</sup> Antony Abhinandan,<sup>‡</sup> Jenny Ardelean,<sup>†</sup> Micheal Scully,<sup>||</sup> Declan Scullion,<sup>||</sup> Lior Embon,<sup>†</sup> Rui Zu,<sup>⊥</sup> Elton J. G. Santos,<sup>||</sup> Luis Balicas,<sup>⊥,#,ID</sup> Chris Marianetti,<sup>▽</sup> Katayun Barmak,<sup>\*,‡</sup> Xiaoyang Zhu,<sup>\*,§,ID</sup> James Hone,<sup>\*,‡</sup> and Abhay N. Pasupathy<sup>\*,†,ID</sup>

<sup>†</sup>Department of Physics, <sup>‡</sup>Department of Mechanical Engineering, and <sup>§</sup>Department of Chemistry, Columbia University, New York, New York 10027, United States

<sup>||</sup>School of Mathematics and Physics, Queen's University, Belfast, BT7 1NN, United Kingdom

<sup>⊥</sup>National High Magnetic Field Laboratory, Florida State University, Tallahassee, Florida 32310, United States

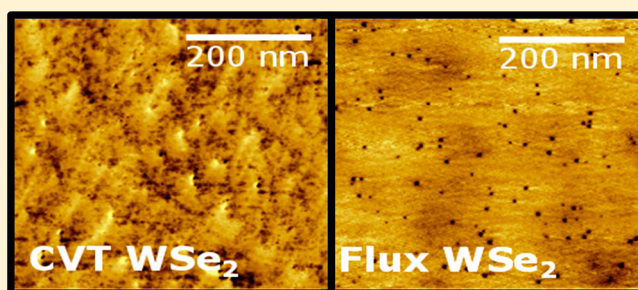
<sup>#</sup>Department of Physics, Florida State University, Tallahassee, Florida 32306, United States

<sup>▽</sup>Department of Applied Physics and Applied Math, Columbia University, New York, New York 10027, United States

## Supporting Information

**ABSTRACT:** Two dimensional (2D) transition-metal dichalcogenide (TMD) based semiconductors have generated intense recent interest due to their novel optical and electronic properties and potential for applications. In this work, we characterize the atomic and electronic nature of intrinsic point defects found in single crystals of these materials synthesized by two different methods, chemical vapor transport and self-flux growth. Using a combination of scanning tunneling microscopy (STM) and scanning transmission electron microscopy (STEM), we show that the two major intrinsic defects in these materials are metal vacancies and chalcogen antisites. We show that by control of the synthetic conditions, we can reduce the defect concentration from above  $10^{13}/\text{cm}^2$  to below  $10^{11}/\text{cm}^2$ . Because these point defects act as centers for nonradiative recombination of excitons, this improvement in material quality leads to a hundred-fold increase in the radiative recombination efficiency

**KEYWORDS:** Transition-metal dichalcogenides, defects, scanning tunneling microscopy, 2D materials



The semiconducting transition metal dichalcogenides (TMDs) are a family of layered compounds with the formula  $\text{MX}_2$  ( $\text{M} = [\text{Mo}, \text{W}]$  and  $\text{X} = [\text{S}, \text{Se}, \text{Te}]$ ), which can be isolated in monolayer form and have promise in a wide range of applications in electronics and optoelectronics.<sup>1–4</sup> These materials host novel phenomena such as valley physics,<sup>5,6</sup> interlayer tunneling,<sup>7,8</sup> topological properties,<sup>9,10</sup> and exciton superfluidity<sup>5</sup> which are of fundamental interest and may enable new device functionality. However, crystalline disorder obscures intrinsic phenomena and imposes an upper limit on achievable functionality.<sup>11,12</sup> In particular, point defects<sup>13–16</sup> strongly impact TMD monolayers; these defects cause carrier scattering and localization,<sup>17–19</sup> act as centers for nonradiative recombination,<sup>20–22</sup> and give rise to localized emission from excitonic traps.<sup>23,24</sup> Pioneering transport<sup>8,25,26</sup> and scanning transmission electron microscopy (STEM) studies<sup>13,14,16</sup> have explored the atomic nature and electronic impact of defects arising in monolayer TMDs and indicate that the quality of these materials remains far behind the classic semiconducting materials such as Si and GaAs. Addressing the

quality of these materials is urgently needed to advance their science and engineering applications.

In two-dimensional materials, disorder can arise from both intrinsic sources, such as point defects and grain boundaries in the crystal itself, and extrinsic sources arising from the environment, such as inhomogeneous strain and charge traps/adsorbates in the substrate.<sup>13</sup> In the case of mechanically exfoliated graphene, the intrinsic defect density is extremely low ( $10^9$ – $10^{10}/\text{cm}^2$ <sup>27,28</sup>), and reducing extrinsic disorder by encapsulation in hexagonal boron nitride (hBN) has enabled spectacular advances in device performance.<sup>29,30</sup> However, other 2D materials do not necessarily possess graphene's ultrahigh purity. In the case of semiconducting TMDs, hBN encapsulation also results in improved performance<sup>31,32</sup> but the physical properties of these devices are still far from their theoretical limits, indicating that intrinsic disorder plays an

**Received:** March 8, 2019

**Revised:** June 3, 2019

**Published:** June 5, 2019

important role. This is consistent with studies showing point defect densities exceeding  $10^{12}/\text{cm}^2$  in commonly used TMD materials.<sup>33</sup> Therefore, continued progress in the field necessitates the characterization, quantification, and minimization of defects in TMD materials. Toward this end, a particular challenge is the diversity of material sources, which include natural or synthesized single crystals, large-area films grown by chemical vapor deposition (CVD),<sup>34,35</sup> metal organic chemical vapor deposition,<sup>36</sup> physical vapor deposition,<sup>37</sup> and molecular beam epitaxy,<sup>38</sup> each of which can give rise to a different density and type of defect. For instance, STEM imaging of  $\text{MoS}_2$  reveals that CVD-grown films are dominated by S-vacancies, whereas defects in natural  $\text{MoS}_2$  crystals are predominantly Mo vacancies.<sup>13</sup>

In this study, we focus on the quality of synthesized TMD single crystals. Currently, single crystals remain the source of the highest-quality TMD monolayers<sup>11</sup> and do not suffer from grain boundaries and phase separation<sup>39,40</sup> observed in large-area films. Although much initial work on TMDs has utilized naturally occurring minerals,<sup>8,41</sup> laboratory-synthesized crystals provide a wider material selection and can offer a higher degree of quality control and reproducibility. Toward this end, a number of companies are currently supplying synthesized TMD crystals for laboratory use. However, synthesized TMD crystals have not been well characterized, and virtually no experimental work has examined the correlation between defect density and optoelectronic properties of monolayers derived from these bulk crystals. In this work, we use scanning tunneling microscopy (STM) and STEM imaging to determine the type and density of intrinsic defects present in single crystals of  $\text{MoSe}_2$  and  $\text{WSe}_2$  synthesized by the chemical vapor transport (CVT) and flux growth techniques. Transition metal vacancies and antisites are found to be the most-common defect types with Se vacancies being much rarer. Flux growth achieves 1–2 orders of magnitude lower defect density than CVT does, and defect densities lower than  $10^{11}/\text{cm}^2$  from our flux-grown sample are by far the lowest reported for TMD materials. This improvement is reflected in reduction of band-edge disorder measured by scanning tunneling spectroscopy, and orders of magnitude increase in photoluminescence quantum yield.

The CVT technique utilizes a transport agent, usually a halogen, to transport starting materials from a hot region into a cooler growth region where they form crystals.<sup>42</sup> CVT provides large crystals in a relatively short growth time at moderate temperatures and thus has become the prevalent technique for TMD synthesis. The self-flux method in which crystals are grown directly from the molten phase is an alternative method known to create higher-quality, albeit smaller, crystals.<sup>43</sup> In this work, we characterize three types of crystals: commercially obtained crystals grown by CVT and tested without further annealing (as-grown CVT or ag-CVT); crystals synthesized in our furnaces by CVT then annealed in a temperature gradient (treated CVT or t-CVT); and crystals grown by the self-flux method (flux). Details of the growth procedures, temperatures, and cooling rates are given in [Methods](#).

We first examine defects in bulk crystals through STM, which can provide defect lattice positions, local electronic structure, and defect density. To avoid surface contamination, crystals were cleaved in situ under ultrahigh vacuum (UHV) conditions. STM imaging of the cleaved surface shows the triangular lattice of the chalcogen atoms that are nearest to the tip. Examining a 25 nm square region of  $\text{MoSe}_2$  ([Figure 1a](#)),

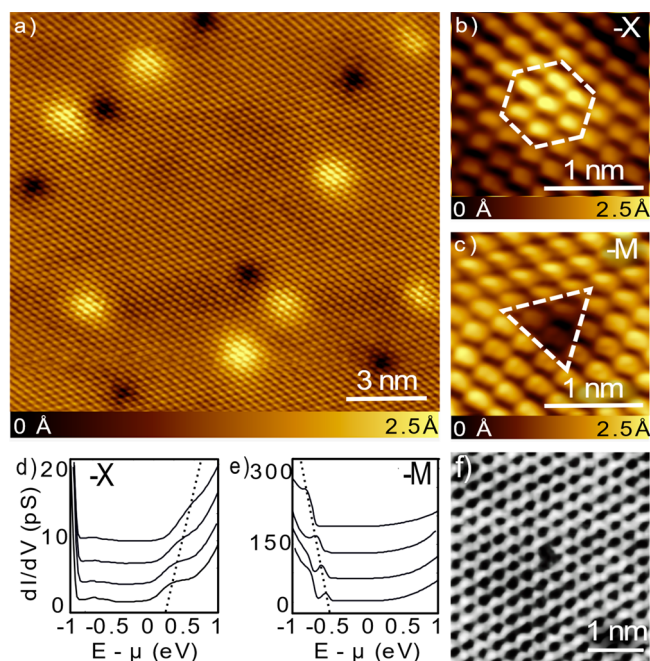


**Figure 1.** Defect atomic and electronic structure high-resolution STM topographic images of  $\text{MoSe}_2$  ( $V = 1.25$  V,  $I = 100$  pA) showing (a) a 25 nm area with two types of defects, (b) a single chalcogen antisite,  $-X$  type defect, and (c) a single metal vacancy,  $-M$  type defect. Differential conductance curves obtained at various distances from a (d) chalcogen antisite, showing the presence of a donor state on the defect site, and (e) single metal vacancy, showing the presence of an acceptor state on the defect site. (f) STEM imaging confirming that  $-M$  defects are metal vacancies.

we observe two defect types that can be initially identified by contrast as either “dark” or “bright”. As discussed further below, these two predominant types of defects account for the vast (>99%) majority of defects imaged in both flux and CVT samples. [Figure 1b,c](#) shows atomic resolution images of these defects. The bright defects, which we denote as  $-X$ , are located on a selenium site ([Figure 1b](#)). Because there is no missing atom associated with this defect, it is not a selenium vacancy<sup>33,44</sup> but is rather a substitutional impurity on the chalcogen site (the atomic site seen to have an atom at all measured scan conditions as seen in [Supporting Information S1](#)). Se vacancies can indeed be observed by STM but are roughly 2 orders of magnitude less common than the vacancies and substitutional impurities (see [Supporting Information Section S2](#) for images of a typical chalcogen vacancy). Further insight into this defect can be obtained by looking at the electronic structure using scanning tunneling spectroscopy (STS). [Figure 1d](#) shows a sequence of tunneling spectra measured at varying distances from a single  $-X$  defect out to a distance of 3.5 nm. Directly over the defect, we measure a broad resonance pinned to the edge of the conduction band. The resonance shifts as a function of distance from the defect site, likely due to band bending effects. This indicates that the  $-X$  defects behave as n-type dopants. STM itself cannot identify the chemical nature of defects. However, we have observed that the concentration of  $-X$  defects can vary widely between crystals depending on the growth method (see below), even when the same starting raw materials are used in the syntheses. This indicates that the defect is not associated with a foreign substituent but is most likely an antisite defect, that is, a Mo atom substituting for a Se atom as suggested by

theoretical calculations (see below). The antisites are observed in roughly equal numbers on the top and bottom selenium layers of the  $\text{MX}_2$  unit cell as expected (see Supporting Information Section S3 for more details).

The dark defects observed in STM images, which we denote  $-M$ , are aligned with the Mo sites, which are located in the center of a triangle of selenium atoms (Figure 1c). In contrast to the  $-X$  defects, the  $-M$  defects show a resonance near the edge of the valence band, as shown in Figure 1e. This indicates that the  $-M$  defects are electron acceptors. Defects spectra are further compared to spectra taken at 10 nm away as shown in Supporting Information S4. Interestingly, whereas flux-grown  $\text{MoSe}_2$  possesses both  $-M$  and  $-X$  defects, similarly grown  $\text{WSe}_2$  displays only  $-M$  defects (see Supporting Information S5 for atomic-resolution images of defects in  $\text{WSe}_2$ ). We note that the apparent heights of the defects that we see in STM images are strongly bias dependent, consistent with previous STM measurements on monolayer TMDs on graphite substrates.<sup>45</sup> Therefore, we have retained a consistent bias for defect counting (again we refer to Supporting Information S1 where bias dependence was examined). This allows direct comparison of defects seen in STM and STEM. In order to perform STEM measurements, we exfoliate flakes of monolayer TMDs which are transferred onto holey carbon substrates as described in Methods. Shown in Figure 1f is an STEM image that shows the only type of point defect observed in the flux-grown  $\text{WSe}_2$  sample (see Supporting Information S6 for addition STEM images). The bright atoms in this image are W due to its high atomic number, indicating that the defect is missing a W atom, that is, a metal vacancy. This chemical assignment of the  $-M$  defect is consistent with the STS observation that they act as electron acceptors.

We quantify the defect density by large-area STM imaging. Figure 2a–c shows topographic scans ( $0.5 \mu\text{m} \times 0.5 \mu\text{m}$ ) of the three  $\text{MoSe}_2$  materials under study. In the ag-CVT sample (Figure 2a), the defect density is high enough such that the individual point defects have overlapping electronic signatures, and therefore STM can only provide a lower bound on the

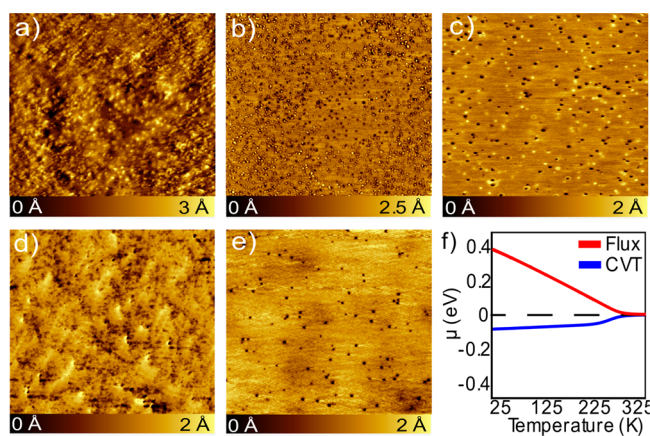


**Figure 2.** Defect density versus growth method in  $\text{MoSe}_2$  and  $\text{WSe}_2$ . STM topographic images of  $500 \times 500 \text{ nm}^2$  areas of a  $\text{MoSe}_2$  crystal grown by (a) commercial as-grown CVT (b) postannealed t-CVT, and (c) self-flux. The imaging conditions for (a–c) were an STM bias of 1.25 V and current of 100 pA. STM topographic images of  $500 \times 500 \text{ nm}^2$  areas of  $\text{WSe}_2$  crystals grown by (d) commercial CVT ( $V = 1 \text{ V}$ ,  $I = 100 \text{ pA}$ ) and (e) self-flux ( $V = 0.75 \text{ V}$ ,  $I = 150 \text{ pA}$ ). (f) Chemical potential calculated from defect densities for  $\text{MoSe}_2$  on treated t-CVT and self-flux crystals as a function of temperature.

defect density of  $>10^{13} \text{ cm}^{-2}$  (1% of unit cells). This defect density is dramatically reduced to  $(2.5 \pm 1.5) \times 10^{12} \text{ cm}^{-2}$  (0.2%) in the t-CVT sample (Figure 2b). The self-flux crystals display still lower defect density of  $(1.7 \pm 0.5) \times 10^{11} \text{ cm}^{-2}$  (0.01%) (Figure 2c). See Supporting Information S7 for defect counting procedures and counts. As for  $\text{MoSe}_2$ , commercial ag-CVT  $\text{WSe}_2$  exhibits a very high defect density and STM imaging can only provide a lower bound of  $>10^{12} \text{ cm}^{-2}$  (0.1%) (Figure 2d). In the flux-grown  $\text{WSe}_2$ , the defect density is dramatically smaller,  $(7.0 \pm 2.2) \times 10^{10} \text{ cm}^{-2}$  (0.006%) (Figure 2e). This defect density is by far the lowest reported for any TMD semiconductor. We additionally sort defect counts by type for each growth method, and a summary of these results for each growth are compared in Table 1. Additional sorting of defects was followed in the Supporting Information S3 regarding the placement of each chalcogen defect within a single TMD layer. We note that in our imaging measurements, clear point defect impurities are only observed from the top  $\text{MX}_2$  layer (as determined by the apparent heights of the defects discussed above). Extended corrugations over larger scales are seen in large scale topographic images such as those shown in Figure 2, which could arise from defects buried between layers<sup>46</sup> or in deeper layers.

Our STM and STS measurements can be compared to theoretical expectations of defect formation energies and electronic structure from density functional theory (DFT). Here we found that a metal vacancy requires an additional 5.22 eV per defect site for its formation (see Methods for definitions of formation energies and chemical potentials). Using the Kröger-Vink (K-V) formalism to examine the chemistry of this defect gives a charge state of  $4^-$  when referenced to the neutral crystal causing this defect type to act as an electron acceptor (i.e.,  $\square_{\text{M}}^{4-} + 4h^\bullet$ , where  $\square_{\text{M}}^{4-}$  denotes the vacancy on the metal site for a compound with chemical formula  $\text{MX}_2$ , this defect has a negative charge relative to the filled metal site in the neutral crystal reference state typically used in the K–V formalism, and  $h^\bullet$  denotes the requisite holes in the valence band to maintain overall charge neutrality). DFT predictions for the local density of states match nicely with the observed STS, finding acceptor states (see Supporting Information S8). The metal antisite defect has a formation energy of 4.81 eV. These defects exhibit a charge state of  $6^+$  when referenced to the neutral crystal making them electron donors, consistent with STM and STS (i.e.,  $\text{M}_{\text{X}}^{6+} + 6e'$  where  $\text{M}_{\text{X}}^{6+}$  denotes the metal antisite and  $e'$  represents the electrons required to retain charge neutrality). Apart from the two observed defect types in experiments, we also calculate the formation energy for chalcogen vacancies. We find this energy to be 1.81 eV, which is lower than that of a metal vacancy or antisite. The observed lack of these vacancies despite their lower formation energy suggests that kinetics plays a large factor in determining observed defect concentrations. Details of these calculations can be found in the methods and a table of calculated values can be seen in the Supporting Information S9. Additional experiments that control for the kinetics of the reaction (for example, by species availability) are required to relate the observed defect concentrations to the formation energies discussed here.

From the observed defect densities and binding energies, we can use semiconductor theory to calculate the chemical potential in various samples of  $\text{MoSe}_2$  as a function of temperature.<sup>47</sup> The result of this calculation is shown in Figure 2f for the t-CVT and flux-grown samples. For the CVT

Table 1. For Each Crystal Studied, Total Defect Density and Distribution of Defect Types<sup>a</sup>

crystal growth method	total defect count defects/cm <sup>2</sup>	M- site defects defects/cm <sup>2</sup>	X- site defects defects/cm <sup>2</sup>
MoSe <sub>2</sub> ag-CVT	>10 <sup>13</sup>	>10 <sup>13</sup>	>10 <sup>13</sup>
MoSe <sub>2</sub> t-CVT	(2.5 ± 1.5) × 10 <sup>12</sup>	(1.3 ± 0.8) × 10 <sup>12</sup>	(1.12 ± 0.6) × 10 <sup>12</sup>
MoSe <sub>2</sub> self-flux	(1.7 ± 0.5) × 10 <sup>11</sup>	(7.0 ± 0.2) × 10 <sup>10</sup>	(9.91 ± 0.2) × 10 <sup>10</sup>
WSe <sub>2</sub> ag-CVT	>10 <sup>12</sup>	>10 <sup>12</sup>	>10 <sup>11</sup>
WSe <sub>2</sub> self-flux	(7.0 ± 2.2) × 10 <sup>10</sup>	(6.41 ± 2.0) × 10 <sup>10</sup>	(5.83 ± 1.8) × 10 <sup>9</sup>

<sup>a</sup>The error bars are from sample to sample variation across different batches of crystals grown by the same growth method. Within a single growth batch, the statistical variations across the crystals are much smaller than the sample-to-sample variations across growth batches.

material, we expect a relatively constant chemical potential due to large but compensated numbers of donor and acceptor defects. The flux-grown crystal, in contrast, has smaller defect density but a dominance of donors, resulting in a strong chemical potential shift toward the conduction band edge as a function of temperature. These considerations indicate that we should measure chemical potential shifts in our STS spectra between different samples. In order to measure this with high spatial resolution, we use STS spectroscopy to measure the local semiconducting gap at every pixel of a 256 × 256 px grid overlaid on a 0.5 × 0.5 μm<sup>2</sup> area. At each point, we extract a local value of the conduction and valence band edges from the local spectrum (see Supporting Information S10 for a detailed description of the procedure). A sum of these two values gives the local value of the semiconducting bandgap.

Shown in Figure 3a is a color scale image of the measured bandgap variation in a t-CVT crystal. Color variations in this

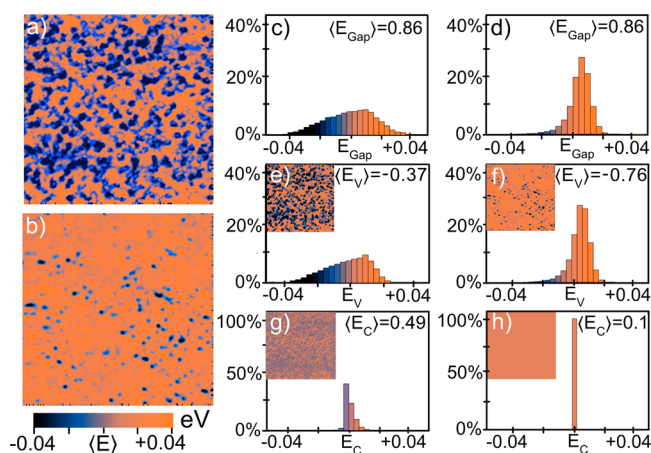


**Figure 3.** Spatially resolved bandgap by scanning tunneling spectroscopy. Map of the semiconducting gap measured on a 256 × 256 pixel grid over a 500 × 500 nm<sup>2</sup> region plotted in the same color scale of (a) post annealed t-CVT and (b) self-flux grown MoSe<sub>2</sub> crystal at 82 K. (c,d) Histograms of bandgap sizes based on (a,b) respectively. Histograms of (e,f) valence band edge and (g,h) conduction band edge from t-CVT and self-flux, respectively. The insets to (e–h) are measured images of the respective band edges in the same color scale.

picture represent gap variations in the vicinity of defects. The average bandgap in this crystal is 860 meV with defect-induced gap variations of the order of 50 meV. The bulk bandgap is in reasonable agreement with the theoretical gap of 840 meV.<sup>48</sup> The variation seen for the t-CVT crystal is to be contrasted with a similar gap variation image for the flux crystal shown in Figure 3b. Although the flux crystal also exhibits an average bandgap of 860 meV, it displays much smaller variations in space due to the lower concentration of defects. To visualize

these differences, histograms detailing the spread of gap sizes for t-CVT and flux are plotted in Figure 3c,d, respectively. The observed gap variation in the t-CVT (3σ) is 50 meV, whereas the flux crystal shows a gap variation of 20 meV. As part of our measurement, STS was able to extract the valence and conduction band edges separately. Therefore, we further the analysis by examining the impact defects have on the valence and conduction band edges. In Figure 3e,f, we plot the valence band onset distributions for t-CVT (centered at −370 meV) and flux (centered at −760 meV), respectively. From these plots, we see that most of the gap variation arises from defect states on the valence edge, which we found earlier correspond to metal vacancies. A similar analysis of the conduction band edge is plotted for t-CVT in Figure 3g (centered at 490 meV) and flux in Figure 3h (centered at 100 meV). Here we see almost no variation, especially in the case of the flux crystal.

Our detailed gap maps can also be used to estimate the position of the chemical potential relative to the gap midpoint from  $\mu = -\frac{\langle E_{\text{C}} \rangle + \langle E_{\text{V}} \rangle}{2}$ . For the t-CVT sample, this gives a chemical potential 60 meV below the gap center, indicating slight p-type doping. The self-flux crystals have a chemical potential of 330 meV above the gap center, making them n-type. At 77 K, we expect from Figure 2f that the chemical potential should be 50 meV below the gap center for t-CVT and 320 meV above the gap center for self-flux. This agreement with STS mapping over a 500 × 500 nm<sup>2</sup> region indicates that we have properly accounted for all of the dopants in the semiconductor. Additionally, the observed behavior explains the commonly observed p-type ambipolar FET devices<sup>49</sup> that have been made from t-CVT crystals. To visualize this further average dI/dV spectra for each bandgap map are presented on the same plot in Supporting Information S11.

To connect the large disparity of crystal imperfections versus growth observed across different crystals in STM to the monolayer limit, we carry out photoluminescence (PL) measurements as a simple way to measure the radiative response versus its quality. We isolate single layers through mechanical exfoliation from bulk single crystals.<sup>32</sup> Monolayers were simultaneously exfoliated from ag-CVT, t-CVT and flux grown crystals and each sample was subsequently handled under identical conditions to eliminate extrinsic factors. Each monolayer was encapsulated in BN and placed on a passivated SiO<sub>2</sub> surface.<sup>31</sup> The resulting stacks were measured under the same conditions (laser excitation power, spot size, and acquisition time). Additional data was taken to ensure that these curves were taken within the linear regime of the laser, as is seen in Supporting Information S12. The raw PL data for MoSe<sub>2</sub> at 4 K are plotted on a log scale in Figure 4a. Whereas the peak position shifts very slightly as crystalline quality is enhanced, the line width (fwhm) shows an obvious decrease with improved crystal quality from 4 meV in ag-CVT to 3 meV

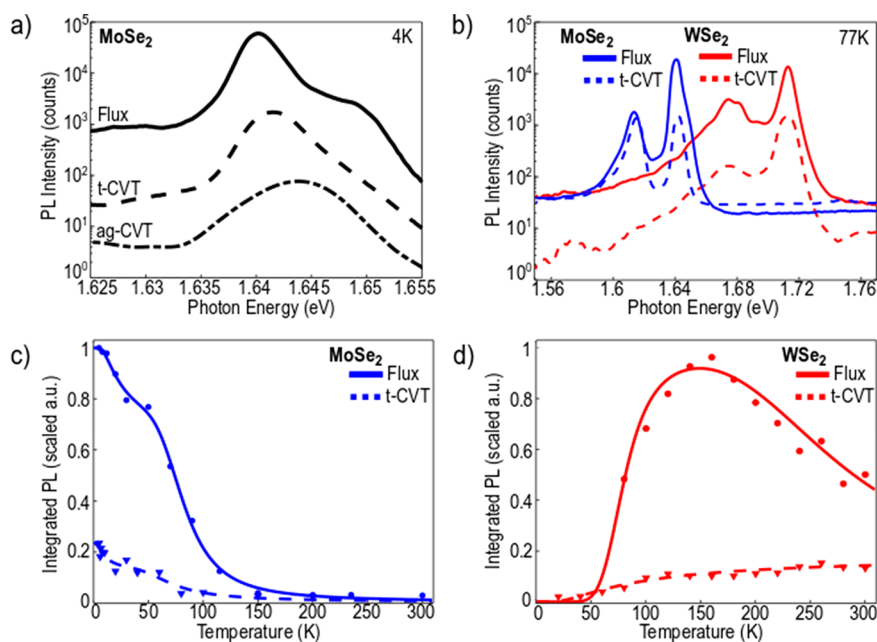


**Figure 4.** Temperature-dependent photoluminescence of monolayer TMDs for different growth methods. (a) PL for ag-CVT, t-CVT, and self-flux grown monolayers of MoSe<sub>2</sub>. All monolayers are encapsulated in h-BN and measured under identical conditions at 4 K. The intensity of the PL from t-CVT and ag-CVT have to be multiplied by 6.7 and 275, respectively, in order to match the peak intensity of the flux-grown monolayer. (b) PL comparing t-CVT (dashed) and self-flux (solid) crystals of MoSe<sub>2</sub> (blue) and WSe<sub>2</sub> (red). (c) Temperature dependence of the integrated PL intensity in MoSe<sub>2</sub> for the full range of incoming photon energies (1.56–1.76 eV) for t-CVT and flux-grown samples. (d) Temperature dependence of the integrated PL intensity (1.56–1.76 eV) in WSe<sub>2</sub> for t-CVT and flux-grown samples. The intensity drop at low temperature is due to the lowest excitonic transition being optically dark. The blue and red lines in (c,d) are fits to a modified Arrhenius form from which the conduction-band splitting can be extracted.

in t-CVT to 2 meV in self-flux sample. The decrease in fwhm is consistent with the improvement in homogeneity of monolayer sample as defect density decreases. A dramatic effect is seen in the total light emission intensity (proportional to the quantum yield) with the self-flux sample having a 10-fold increase in light intensity over the t-CVT monolayer, and a 100-fold increase over the ag-CVT monolayer. We note that improvements in PL yield can also be achieved by various surface treatments<sup>50,51</sup> that can affect the exciton lifetime or light absorption. In our PL experiments, we take care to keep the environment of the films as identical as possible across samples via encapsulation in BN. Our measurements are also performed in the linear regime as shown in the Supporting Information. The large suppression of excitons with little change to peak position suggests that defects provide nonradiative pathways for the recombination of excitons, via exciton localization<sup>52</sup> or defect-enhanced Auger processes,<sup>20,22</sup> lowering the PL yield from the intrinsic limit of a pristine sample.

To quantify the impact of defects on the excitonic properties, we extend the PL measurements described above to various temperatures on t-CVT and flux monolayers (ag-CVT is omitted due to a lack of intensity at high temperatures). We plot the data taken for both MoSe<sub>2</sub> (red) and WSe<sub>2</sub> (blue) on a log scale at 77 K in Figure 4b where t-CVT is a dashed line and flux is a solid line. Because the major observed difference from the crystals is the overall PL intensity, we plot the integrated PL intensity as seen for MoSe<sub>2</sub> in Figure 4c. To model the shape of the integrated PL signal we must account for the unique band structure of monolayer TMDs. In the TMD materials, both the valence and conduction bands are spin split due to spin–orbit coupling. The magnitude of the

splitting in the valence band is roughly an order of magnitude larger than the conduction-band splitting (~300 meV versus ~30 meV). Because of the spin splitting in the conduction band, one of the two transitions from the conduction band to the upper valence band (A exciton) is dark, whereas the other is optically bright. In MoSe<sub>2</sub> the lower of the two transitions is bright, while the situation is reversed in WSe<sub>2</sub>. We fit the integrated PL intensity to an empirical Arrhenius equation, which accounts for both the spin split exciton,<sup>53</sup> and nonradiative processes which average multiple recombination rates. The full analysis followed is described in the Supporting Information S13. We find that the integrated PL emission can be described as follows for MoSe<sub>2</sub>

$$I_{\text{Tot}} = \frac{1}{1 + C_1 * e^{-\Delta E_{\text{NR}}/k_B T} + C_2 * e^{-\Delta E_{\text{Dark}}/k_B T}}$$

Here the nonradiative term arises both from defects and phonon scattering at higher temperatures, and other term arises from thermal equilibrium between the dark and bright excitons. In Figure 4c, a sudden drop can be seen in the PL signal of the self-flux MoSe<sub>2</sub> monolayer above roughly 60 K. This can be attributed to the Boltzmann distribution of electrons able to access the dark exciton state. As per our fit prescribed above, we extract the dark exciton energy to be 40 meV above the bright exciton binding energy. This matches well with reports utilizing a backgate to directly measure the dark exciton at 30 meV above the bright one.<sup>54</sup>

Like MoSe<sub>2</sub>, the PL resonances of WSe<sub>2</sub> have roughly the same peak position across growth methods. The temperature-dependent integrated intensity shows distinct behaviors for the flux versus CVT crystals as shown in Figure 4d. The self-flux crystal shows an initial increase in the PL intensity with

decreasing temperature down to about 150 K, below which the intensity drops sharply. The CVT crystal however shows a decreasing intensity with decreasing temperature starting from room temperature. This difference in the case of WSe<sub>2</sub> arises due to the fact that the lowest energy transition is dark.<sup>55</sup> This implies that at sufficiently low temperature only the dark state is populated, exponentially suppressing the PL intensity. At high enough temperature, on the other hand, the PL intensity is suppressed with increasing temperature due to phonon scattering. We can model both effects together using the same formula as MoSe<sub>2</sub> with a sign change

$$I_{\text{Tot}} = \frac{1}{1 + C_1 * e^{-\Delta E_{\text{NR}}/k_B T} + C_2 * e^{\Delta E_{\text{Dark}}/k_B T}}$$

This change of sign indicates that the dark exciton is now at a lower energy than the bright. Thus, PL shows a maximum at some intermediate temperature which is determined by the interplay between defect and phonon recombination versus dark exciton coupling. Using the fitting for the integrated intensity from the flux crystal, we extract a conduction-band splitting of 43 meV. Our measurement of this splitting is within experimental error of the value directly measured from magnetic field measurements (47 meV).<sup>56,57</sup> We additionally find that CVT crystals exhibit stronger defect-mediated coupling to the dark exciton state diminishing the PL signal out to much higher temperatures.

Our studies of defects in transition-metal dichalcogenides show definitively that there is a direct link between intrinsic point defect concentration in bulk crystals and the optoelectronic properties of exfoliated monolayers. The improvements in synthesis presented here have led to a lowering of the defect concentration by 2 orders of magnitude when compared to the current state of the art. Such improvements are a necessary step toward achieving many of the predicted optical phenomena that require high exciton concentration as well as transport phenomena that require long scattering times. We note in conclusion that although our synthetic achievements set a new benchmark for TMD semiconductors, the lowest bulk defect concentrations achieved here ( $\sim 10^{18}/\text{cm}^3$ ) are still significantly higher than those achieved in the best III–V semiconductor films, indicating that there is still room for refining synthetic processes to achieve higher quality TMD materials.

**Methods. Flux Growth.** MoSe<sub>2</sub> and WSe<sub>2</sub> crystals were synthesized by reacting Mo/W powders, 99.999%, with a Se shot, 99.999%, typically in a ratio of 1:20. These materials were first loaded into a quartz ampule. A piece of quartz wool is then pressed into a cylindrical shape and pushed into the quartz ampule, approximately 1 cm above the raw elements. The ampule was then evacuated and sealed at  $\sim 10^{-3}$  Torr. For growth, the ampule is heated to 1000 °C over 48 h, held there for 3 days, then cooled at a rate of 1.5 °C down to 400 °C and subsequently flipped and centrifuged. Crystals are then harvested from the quartz wool filter and annealed at a temperature of 250 °C with the empty end of the quartz ampule held approximately at 100 °C for 48 h.

**CVT.** MoSe<sub>2</sub> crystals were synthesized by reacting Mo powder, 99.999%, with a Se shot, 99.999%, in stoichiometric proportions with iodine 99.999% as a transport agent. These materials were first loaded into a quartz ampule, 12 cm in length and 1 cm in diameter, then evacuated and sealed at  $\sim 10^{-3}$  Torr. For growth, the ampule is heated to 1000 °C over

a period of 48 h, held there for 1 week, then cooled for 3 days to 750 °C and subsequently quenched in air. Crystals are then harvested and rinsed in acetone and isopropanol to remove iodine residue and left to dry.

**Ab Initio Density Functional Theory Methods.** First-principle calculations for defect formation energies were done using density functional theory (DFT) within the projected augmented wave method,<sup>58,59</sup> as implemented in the VASP code.<sup>60,61</sup> The generalized gradient approximation<sup>62</sup> is employed to treat exchange and correlation in DFT. Projected augmented wave method (PAW) was used in the description of the bonding environment for W, Mo, and Se. The structures are fully relaxed until all interatomic forces are smaller than 0.02 eV/Å. The Brillouin zone was sampled with a  $5 \times 5 \times 1$  k-mesh under the Monkhorst–Pack scheme.<sup>63</sup> Plane-wave energy cut offs of 400 and 500 eV are used for structural relaxation and static runs, respectively. The defect formation energies are defined via  $E_{\text{form}} = E_{\text{defect}} - (E_{\text{pristine}} + \sum n_i \mu_i)$ , where  $E_{\text{defect}}$  stands for the total energy of a defected monolayer,  $E_{\text{pristine}}$  is the total energy of a pristine monolayer,  $n_i$  is the number of removed (minus sign) or added (plus sign) species  $i$  and  $\mu_i$  is the chemical potential of species  $i$ . The size of the supercell was determined by convergence tests, resulting in a  $6 \times 6 \times 1$  with a 15 Å vacuum space. The chemical potentials of each species are constrained by the relation,<sup>63</sup>  $\mu_{\text{MoSe}_2} = \mu_{\text{Mo}} + 2 \mu_{\text{Se}}$ , where  $\mu_{\text{Mo}}$  and  $\mu_{\text{Se}}$  are the chemical potentials for Mo and Se, respectively;  $\mu_{\text{MoSe}_2}$  is the total energy per formula unit of MoSe<sub>2</sub>. We determine the range of chemical potentials with two extreme cases: Mo-rich environment and Se-rich environment. For the Mo-rich environment,  $\mu_{\text{Mo}}$  is chosen to be the total energy per atom of Mo in the body-centered cubic structure. For the Se-rich environment,  $\mu_{\text{Se}}$  is chosen to be the total energy per atom of Se in the trigonal phase. The defect formation energies as a function of  $\mu_{\text{Mo}}$  are presented in the Supporting Information S7. The values in the main text are extracted with the chemical potentials following  $\mu_i = E_i + E_{\text{bond}}$ , where  $E_i$  = Total energy of bulk metal or crystal of chalcogenide and  $E_{\text{bond}} = (E_{\text{MX}_2} - E_{\text{M}} - 2E_{\text{X}})/3$ .<sup>64</sup>

**Scanning Tunneling Microscopy and Spectroscopy (STM).** STM measurements were performed using a custom built, variable temperature, UHV STM system. Single crystals of MoSe<sub>2</sub> and WSe<sub>2</sub> were mounted onto metallic sample holders using a vacuum safe silver paste. Samples were then transferred into the STM chamber and cleaved in situ, exposing a clean surface. A Pt–Ir STM tip was cleaned and calibrated against a gold (111) single crystal prior to the measurements. Measurements were collected at 82 and 300 K.

**Optical Measurements.** Optical stacks of BN/TMD/BN were fabricated using the polypropylene carbonate (PPC) method as described in ref 65 and placed on passivated SiO<sub>2</sub>.<sup>31</sup> MoSe<sub>2</sub> samples were measured using a closed-cycle He cryostat (Attocube Attodry 1100) and an excitation wavelength of 532 nm using a cw diode laser with an approximate power of 2.0 μW. For WSe<sub>2</sub>, samples were loaded into a cryostat with a sapphire window which is combined with a homemade photoluminescence setup with an excitation wavelength of 532 nm using a cw diode laser and a power of 80 μW. For cooling, either helium-4 or liquid nitrogen were continuously flowed through the cryostat chamber, immersing the sample while temperature was modulated with a stage heater.

*Transmission Electron Microscope (TEM) Sample Preparation and Scanning Transmission Electron Microscope (STEM) Imaging.* For the preparation of electron transparent samples for point defect density measurements, the TMD crystals were mechanically exfoliated using Scotch tape. The exfoliated flakes were transferred onto oxidized silicon wafer substrates. The monolayer flakes of the exfoliated TMD crystals were identified using light optical microscopy. The monolayers were then transferred onto Quantifoil holey carbon TEM grids using isopropyl alcohol as a medium. After the alcohol evaporated, the holey carbon grid was attached to the wafer and the monolayer. The wafer sections were then slowly immersed in 1 M potassium hydroxide (KOH) solution to etch the very top surface of the oxide and release the TEM grid and the exfoliated crystals attached to it. Distilled water was used to dilute and wash away the KOH solution from the TEM grids. As a last step, TEM grids were immersed in warm (40 °C) acetone for 10 min to dissolve any residue that remained from the exfoliation and sample transfer.

The STEM imaging of TMD monolayers was carried out in an FEI Talos F200X instrument operated at 200 kV. A low beam current (~60 pA) was used to reduce the amount of beam damage. By using the smallest condenser aperture (50 μm) and beam size of 9, the convergence angle of the probe was calculated to be approximately 10 mrad. Images were acquired at a series of times to determine the rate at which metal vacancies formed in the samples when irradiated by the electron beam. For MoSe<sub>2</sub>, the density of metal vacancies was found to increase linearly with time allowing extrapolation to time zero to determine the initial density. For WSe<sub>2</sub>, no new metal vacancies were found to be created up to 40 s of imaging. Thus, for these samples, images from multiple regions were collected using a 20 s acquisition time. To improve the contrast and reduce the noise in the images for quantification of point defect density, the Butterworth filter in Gatan Digital Micrograph and the Wiener deconvolution in MATLAB were used. In addition, the simulated structure of the monolayer using the CrystalMaker software was overlaid on the processed STEM images to aid in identification of the metal and the chalcogen positions.

## ■ ASSOCIATED CONTENT

### ● Supporting Information

The Supporting Information is available free of charge on the ACS Publications website at DOI: 10.1021/acs.nanolett.9b00985.

Additional information, figures, and table (PDF)

## ■ AUTHOR INFORMATION

### Corresponding Authors

\*E-mail: apn2108@columbia.edu.

\*E-mail: jh2228@columbia.edu.

\*E-mail: xyzhu@columbia.edu.

\*E-mail: kb2612@columbia.edu.

### ORCID

Jue Wang: 0000-0001-6843-9771

Luis Balicas: 0000-0002-5209-0293

Xiaoyang Zhu: 0000-0002-2090-8484

Abhay N. Pasupathy: 0000-0002-2744-0634

### Author Contributions

○D.E. and D.R. contributed equally to this work

## Funding

This work is supported by the NSF MRSEC program through Columbia in the Center for Precision Assembly of Superstratic and Superatomic Solids (DMR-1420634). Support for STM instrumentation is provided by the Air Force Office of Scientific Research (Grant FA9550-16-1-0601). K.B. and A.Z. acknowledge partial funding support from the Dean of the School of Engineering and Applied Science at Columbia University. D.S. acknowledges his EPSRC studentship. E.J.G.S. acknowledges the use of computational resources from the U.K. national high-performance computing service (ARCHER) for which access was obtained via the UKCP consortium (EPSRC Grant EP/K013564/1); the U.K. Materials and Molecular Modeling Hub for access to THOMAS, which is partially funded by EPSRC (EP/P020194/1). E.J.G.S. also acknowledges the Queen's Fellow Award through the Grant M8407MPH, the Enabling Fund (A5047TSL), and the Department for the Economy (USI 097). L.B. acknowledges the U.S. Army Research Office MURI Grant W911NF-11-1-0362 (Synthesis and Physical Characterization of Two-Dimensional Materials and Their Heterostructures) and the Office Naval Research DURIP Grant 11997003 (Stacking Under Inert Conditions). Preliminary growth and characterization single crystals were performed at the National High Magnetic Field Laboratory, which is supported by the NSF Cooperative Agreement DMR-1157490 and the State of Florida.

## Notes

The authors declare no competing financial interest.

## ■ ACKNOWLEDGMENTS

Yinan Dong, Bryan Medina, and Steven French are acknowledged for their assistance in sample preparation.

## ■ ABBREVIATIONS

TMD, transition metal dichalcogenide; CVT, chemical vapor transport; STM, scanning tunneling microscopy; STS, scanning tunneling spectroscopy; STEM, scanning transmission electron microscopy; DFT, density functional theory; PL, photoluminescence.

## ■ REFERENCES

- (1) Chen, X.; Yan, T.; Zhu, B.; Yang, S.; Cui, X. Optical Control of Spin Polarization in Monolayer Transition Metal Dichalcogenides. *ACS Nano* **2017**, *11*, 1581.
- (2) Lee, J.; Mak, K. F.; Shan, J. Electrical control of the valley Hall effect in bilayer MoS<sub>2</sub> transistors. *Nat. Nanotechnol.* **2016**, *11*, 421–425.
- (3) Mak, K. F.; Shan, J. Photonics and optoelectronics of 2D semiconductor transition metal dichalcogenides. *Nat. Photonics* **2016**, *10*, 216–226.
- (4) Xu, X.; Yao, W.; Xiao, D.; Heinz, T. F. Spin and pseudospins in layered transition metal dichalcogenides. *Nat. Phys.* **2014**, *10*, 343–350.
- (5) Fogler, M.; Butov, L.; Novoselov, K. High-temperature superfluidity with indirect excitons in van der Waals heterostructures. *Nat. Commun.* **2014**, *5*, 4555.
- (6) Sie, E. J.; Frenzel, A. J.; Lee, Y.-H.; Kong, J.; Gedik, N. Intervalley biexcitons and many-body effects in monolayer  $\text{MoS}_2$ . *Phys. Rev. B: Condens. Matter Mater. Phys.* **2015**, *92*, 125417.
- (7) Ma, N.; Jena, D. Interband tunneling in two-dimensional crystal semiconductors. *Appl. Phys. Lett.* **2013**, *102*, 132102.

- (8) Radisavljevic, B.; Radenovic, A.; Brivio, J.; Giacometti, V.; Kis, A. Single-layer MoS<sub>2</sub> transistors. *Nat. Nanotechnol.* **2011**, *6*, 147–150.
- (9) Bruno, F. Y.; et al. Observation of large topologically trivial Fermi arcs in the candidate type-II Weyl semimetal  $\text{WTe}_2$ . *Phys. Rev. B: Condens. Matter Mater. Phys.* **2016**, *94*, 121112.
- (10) Soluyanov, A. A.; et al. Type-II Weyl semimetals. *Nature* **2015**, *527*, 495.
- (11) Choi, W.; et al. Recent development of two-dimensional transition metal dichalcogenides and their applications. *Mater. Today* **2017**, *20*, 116–130.
- (12) Zeng, Q.; Liu, Z. Novel Optoelectronic Devices: Transition-Metal-Dichalcogenide-Based 2D Heterostructures. *Adv. Electron. Mater.* **2018**, *4*, 1700335.
- (13) Hong, J. Exploring atomic defects in molybdenum disulfide monolayers. *Nat. Commun.* **2015**, *6*, 7293 DOI: 10.1038/ncomms7293.
- (14) Lin, Z.; et al. Defect engineering of two-dimensional transition metal dichalcogenides. *2D Mater.* **2016**, *3*, 022002.
- (15) Yankowitz, M.; McKenzie, D.; LeRoy, B. J. Local Spectroscopic Characterization of Spin and Layer Polarization in  $\text{WSe}_2$ . *Phys. Rev. Lett.* **2015**, *115*, 136803.
- (16) Zhou, W.; et al. Intrinsic structural defects in monolayer molybdenum disulfide. *Nano Lett.* **2013**, *13*, 2615–2622.
- (17) El-Mahalawy, S.; Evans, B. Temperature dependence of the electrical conductivity and hall coefficient in 2H-MoS<sub>2</sub>, MoSe<sub>2</sub>, WSe<sub>2</sub>, and MoTe<sub>2</sub>. *Phys. Status Solidi B* **1977**, *79*, 713–722.
- (18) Fivaz, R.; Mooser, E. Mobility of charge carriers in semiconducting layer structures. *Phys. Rev.* **1967**, *163*, 743.
- (19) Walukiewicz, W. Carrier scattering by native defects in heavily doped semiconductors. *Phys. Rev. B: Condens. Matter Mater. Phys.* **1990**, *41*, 10218.
- (20) Moody, G.; Schaibley, J.; Xu, X. Exciton dynamics in monolayer transition metal dichalcogenides [Invited]. *J. Opt. Soc. Am. B* **2016**, *33*, C39–C49.
- (21) Palummo, M.; Bernardi, M.; Grossman, J. C. Exciton radiative lifetimes in two-dimensional transition metal dichalcogenides. *Nano Lett.* **2015**, *15*, 2794–2800.
- (22) Wang, H.; Zhang, C.; Rana, F. Ultrafast dynamics of defect-assisted electron–hole recombination in monolayer MoS<sub>2</sub>. *Nano Lett.* **2015**, *15*, 339–345.
- (23) Bastard, G.; Delalande, C.; Meynadier, M.; Frijlink, P.; Voos, M. Low-temperature exciton trapping on interface defects in semiconductor quantum wells. *Phys. Rev. B: Condens. Matter Mater. Phys.* **1984**, *29*, 7042.
- (24) Ky, N. H.; Reinhart, F. Amphoteric native defect reactions in Si-doped GaAs. *J. Appl. Phys.* **1998**, *83*, 718–724.
- (25) Baugher, B. W. H.; Churchill, H. O. H.; Yang, Y.; Jarillo-Herrero, P. Intrinsic Electronic Transport Properties of High-Quality Monolayer and Bilayer MoS<sub>2</sub>. *Nano Lett.* **2013**, *13*, 4212–4216.
- (26) Ovchinnikov, D.; Allain, A.; Huang, Y.-S.; Dumcenco, D.; Kis, A. Electrical transport properties of single-layer WS<sub>2</sub>. *ACS Nano* **2014**, *8*, 8174–8181.
- (27) Liu, L.; Qing, M.; Wang, Y.; Chen, S. Defects in Graphene: Generation, Healing, and Their Effects on the Properties of Graphene: A Review. *J. Mater. Sci. Technol.* **2015**, *31*, 599–606.
- (28) Zhong, J.-H.; et al. Quantitative Correlation between Defect Density and Heterogeneous Electron Transfer Rate of Single Layer Graphene. *J. Am. Chem. Soc.* **2014**, *136*, 16609–16617.
- (29) Dean, C. R.; et al. Boron nitride substrates for high-quality graphene electronics. *Nat. Nanotechnol.* **2010**, *5*, 722–726.
- (30) Mayorov, A. S.; et al. Micrometer-scale ballistic transport in encapsulated graphene at room temperature. *Nano Lett.* **2011**, *11*, 2396–2399.
- (31) Ajayi, O. Approaching the Intrinsic Photoluminescence Linewidth in Transition Metal Dichalcogenide Monolayers. *2D Mater.* **2017**, *4*, 031011.
- (32) Wang, J. I.-J.; et al. Electronic transport of encapsulated graphene and WSe<sub>2</sub> devices fabricated by pick-up of prepatterned hBN. *Nano Lett.* **2015**, *15*, 1898–1903.
- (33) McDonnell, S.; Addou, R.; Buie, C.; Wallace, R. M.; Hinkle, C. L. Defect-dominated doping and contact resistance in MoS<sub>2</sub>. *ACS Nano* **2014**, *8*, 2880–2888.
- (34) Chen, J. Chemical Vapor Deposition of Large-size Monolayer MoSe<sub>2</sub> Crystals on Molten Glass. *J. Am. Chem. Soc.* **2017**, *139*, 13476.
- (35) Lee, Y. H.; et al. Synthesis of Large-Area MoS<sub>2</sub> Atomic Layers with Chemical Vapor Deposition. *Adv. Mater.* **2012**, *24*, 2320–2325.
- (36) Eichfeld, S. M.; et al. Highly scalable, atomically thin WSe<sub>2</sub> grown via metal–organic chemical vapor deposition. *ACS Nano* **2015**, *9*, 2080–2087.
- (37) Muratore, C.; et al. Continuous ultra-thin MoS<sub>2</sub> films grown by low-temperature physical vapor deposition. *Appl. Phys. Lett.* **2014**, *104*, 261604.
- (38) Zhang, Y.; et al. Direct observation of the transition from indirect to direct bandgap in atomically thin epitaxial MoSe<sub>2</sub>. *Nat. Nanotechnol.* **2014**, *9*, 111–115.
- (39) Kang, K.; et al. High-mobility three-atom-thick semiconducting films with wafer-scale homogeneity. *Nature* **2015**, *520*, 656.
- (40) Van Der Zande, A. M.; et al. Grains and grain boundaries in highly crystalline monolayer molybdenum disulfide. *Nat. Mater.* **2013**, *12*, 554–561.
- (41) Manzeli, S.; Ovchinnikov, D.; Pasquier, D.; Yazyev, O. V.; Kis, A. 2D transition metal dichalcogenides. *Nat. Rev.* **2017**, *2*, 17033.
- (42) Ubaldini, A.; Jacimovic, J.; Ubrig, N.; Giannini, E. Chloride-Driven Chemical Vapor Transport Method for Crystal Growth of Transition Metal Dichalcogenides. *Cryst. Growth Des.* **2013**, *13*, 4453–4459.
- (43) Zhang, X.; et al. Flux method growth of bulk MoS<sub>2</sub> single crystals and their application as a saturable absorber. *CrystEngComm* **2015**, *17*, 4026–4032.
- (44) Voiry, D.; Mohite, A.; Chhowalla, M. Phase engineering of transition metal dichalcogenides. *Chem. Soc. Rev.* **2015**, *44*, 2702–2712.
- (45) Zhang, S.; et al. Defect Structure of Localized Excitons in a  $\text{WSe}_2$  Monolayer. *Phys. Rev. Lett.* **2017**, *119*, 046101.
- (46) Lu, C.-P.; Li, G.; Mao, J.; Wang, L.-M.; Andrei, E. Y. Bandgap, Mid-Gap States, and Gating Effects in MoS<sub>2</sub>. *Nano Lett.* **2014**, *14*, 4628–4633.
- (47) Jin, Z.; Li, X.; Mullen, J. T.; Kim, K. W. Intrinsic transport properties of electrons and holes in monolayer transition-metal dichalcogenides. *Phys. Rev. B: Condens. Matter Mater. Phys.* **2014**, *90*, 045422.
- (48) Tongay, S.; et al. Thermally Driven Crossover from Indirect toward Direct Bandgap in 2D Semiconductors: MoSe<sub>2</sub> versus MoS<sub>2</sub>. *Nano Lett.* **2012**, *12*, 5576–5580.
- (49) Pradhan, N. R.; et al. Ambipolar molybdenum diselenide field-effect transistors: field-effect and hall mobilities. *ACS Nano* **2014**, *8*, 7923–7929.
- (50) Amani, M.; et al. High Luminescence Efficiency in MoS<sub>2</sub> Grown by Chemical Vapor Deposition. *ACS Nano* **2016**, *10*, 6535–6541.
- (51) Amani, M.; et al. Near-unity photoluminescence quantum yield in MoS<sub>2</sub>. *Science* **2015**, *350*, 1065.
- (52) Godde, T.; et al. Exciton and trion dynamics in atomically thin MoSe<sub>2</sub> and WSe<sub>2</sub>: Effect of localization. *Phys. Rev. B: Condens. Matter Mater. Phys.* **2016**, *94*, 165301.
- (53) Baranowski, M.; et al. Dark excitons and the elusive valley polarization in transition metal dichalcogenides. *2D Mater.* **2017**, *4*, 025016.
- (54) Quereda, J.; Ghiasi, T. S.; van Zwol, F. A.; van der Wal, C. H.; van Wees, B. J. Observation of bright and dark exciton transitions in monolayer MoSe<sub>2</sub> by photocurrent spectroscopy. *2D Mater.* **2018**, *5*, 015004.



- (55) Dery, H.; Song, Y. Polarization analysis of excitons in monolayer and bilayer transition-metal dichalcogenides. *Phys. Rev. B: Condens. Matter Mater. Phys.* **2015**, *92*, 125431.
- (56) Wang, G.; et al. Magneto-optics in transition metal diselenide monolayers. *2D Mater.* **2015**, *2*, 034002.
- (57) Zhang, X.-X.; You, Y.; Zhao, S. Y. F.; Heinz, T. F. Experimental evidence for dark excitons in monolayer WSe<sub>2</sub>. *Phys. Rev. Lett.* **2015**, *115*, 257403.
- (58) Kresse, G.; Furthmüller, J. Efficient iterative schemes for ab initio total-energy calculations using a plane-wave basis set. *Phys. Rev. B: Condens. Matter Mater. Phys.* **1996**, *54*, 11169–11186.
- (59) Kresse, G.; Hafner, J. Ab initio molecular dynamics for open-shell transition metals. *Phys. Rev. B: Condens. Matter Mater. Phys.* **1993**, *48*, 13115–13118.
- (60) Blöchl, P. E. Projector augmented-wave method. *Phys. Rev. B: Condens. Matter Mater. Phys.* **1994**, *50*, 17953–17979.
- (61) Perdew, J. P.; Burke, K.; Ernzerhof, M. Generalized Gradient Approximation Made Simple. *Phys. Rev. Lett.* **1996**, *77*, 3865–3868.
- (62) Kresse, G.; Joubert, D. From ultrasoft pseudopotentials to the projector augmented-wave method. *Phys. Rev. B: Condens. Matter Mater. Phys.* **1999**, *59*, 1758–1775.
- (63) Monkhorst, H. J.; Pack, J. D. Special points for Brillouin-zone integrations. *Phys. Rev. B* **1976**, *13*, 5188–5192.
- (64) Haldar, S.; Vovusha, H.; Yadav, M. K.; Eriksson, O.; Sanyal, B. Systematic study of structural, electronic, and optical properties of atomic-scale defects in the two-dimensional transition metal dichalcogenides  $M_{2}X_2$  ( $M = \text{Mo}$ ,  $W$ ;  $X = \text{S}$ ,  $\text{Se}$ ,  $\text{Te}$ ). *Phys. Rev. B: Condens. Matter Mater. Phys.* **2015**, *92*, 235408.
- (65) Wang, L.; et al. One-dimensional electrical contact to a two-dimensional material. *Science* **2013**, *342*, 614–617.